

Moiré folded helical states at the interfaces of heterostructures

Paula Mellado¹

¹Facultad de Ingeniería y Ciencias,
Universidad Adolfo Ibáñez, Santiago, Chile.

(Dated: February 2, 2026)

A minimal model of a graphene-topological-insulator heterostructure is considered, where a moiré superlattice modulates the Rashba spin-orbit interaction (SOC). In the spin-degenerate, spin-orbit-free limit, the reduced Brillouin zone contains flat, spin-degenerate moiré minibands, with periodicity determined by superlattice folding. The inclusion of SOC lifts the spin degeneracy and reduces the effective spectral periodicity by a factor of two. Through SOC, the moiré potential entangles spin, sublattice, and leg degrees of freedom, reshaping the miniband structure in momentum space and generating emergent helicity spectral functions. As the Rashba coupling is renormalized by the moiré pattern, it induces helicity fragmentation, in which the helicity weight is distributed across a dense manifold of moiré minibands, forming an extended network of helicity-carrying states and significantly enhancing helicity fluctuations at the bare-response level. The emergence of Dirac-like miniband crossings at finite SOC demonstrates that moiré heterostructures can support relativistic quasiparticles through band reconstruction. This model provides a microscopic mechanism by which proximity-induced spin-orbit coupling can be amplified via moiré engineering.

I. INTRODUCTION

Materials with intrinsically weak spin-orbit coupling (SOC) do not exhibit spin-momentum locking or spin-driven collective states [1]. An essential approach to introduce SOC into high-mobility systems is to exploit proximity effects in van der Waals heterostructures, which allows a low-SOC material to inherit SOC from an adjacent strong-SOC layer [2]. In van der Waals heterostructures, interfacial spin-orbit coupling originates from broken inversion symmetry combined with strong atomic SOC in one of the constituent layers. In this regard, graphene/three-dimensional topological insulator (TI) heterostructures are promising, as they combine Dirac quasiparticles, strong spin-momentum locking, adjustable electrostatics, and atomically clean interfaces [3]. Experimental and theoretical investigations of graphene/TI heterostructures have shown that the TI surface states can impart strong SOC to graphene, producing spin splitting, anisotropic spin textures, and gate-controllable helical behavior [4, 5]. Tight-binding and ab initio calculations reveal that the induced SOC is highly sensitive to interface symmetry, stacking configuration, and sublattice alignment, typically producing a complex combination of Rashba, valley-Zeeman, and pseudospin-dependent SOC terms [6–8]. Despite these advances, a central unresolved question is whether the observed SOC simply reflects a passive inheritance of the TI’s spin texture, or whether it can instead be actively enhanced and reprogrammed via additional interfacial structural modulations [9–11].

A promising approach to address this issue considers the formation of a moiré superlattice at the graphene-topological insulator (TI) interface. Such moiré pattern can be induced by lattice mismatch, relative twist, or commensurate stacking over large unit cells [12]. It has been shown in several twisted heterostructures that moiré patterns produce flattened electronic

minibands and enhance interband hybridization, thereby amplifying correlation effects [13]. In several graphene moiré platforms, including twisted bilayer graphene [14] and graphene on transition-metal dichalcogenides [15], such effects are known to substantially modify electronic, magnetic, and topological characteristics [16]. In TI/graphene heterostructures, where proximity already endows graphene with spin-orbit coupling [17], the moiré pattern produces spatially varying interlayer and intersublattice hybridization that can couple strongly to spin-orbit effects [18, 19].

In this article, we introduce a minimal model that isolates the combined effects of proximity-induced SOC and moiré-modulated interband hopping in graphene (Gr)-based heterostructures. Rather than focusing on material specific details, we employ a toy model approach inspired by recent works on moiré ladders and incommensurate heterostructures [20–22]. We investigate how moiré modulation influences a spin-orbit-coupled heterostructure, focusing on whether the moiré potential can enhance spin-momentum locking and promote the emergence of a collective instability in the system. To that end, we characterize the dominant fluctuation channels of this system, focusing on helicity rather than conventional charge or spin order. We analyze the bare susceptibilities associated with helicity density and helicity current operators. We show that while helicity spectral functions vanish in the absence of SOC, the static susceptibilities become strongly enhanced once SOC and moiré hybridization coexist. Our results open a new route toward designing helical and spin orbit driven phases in van der Waals heterostructures through controlled structural modulation.

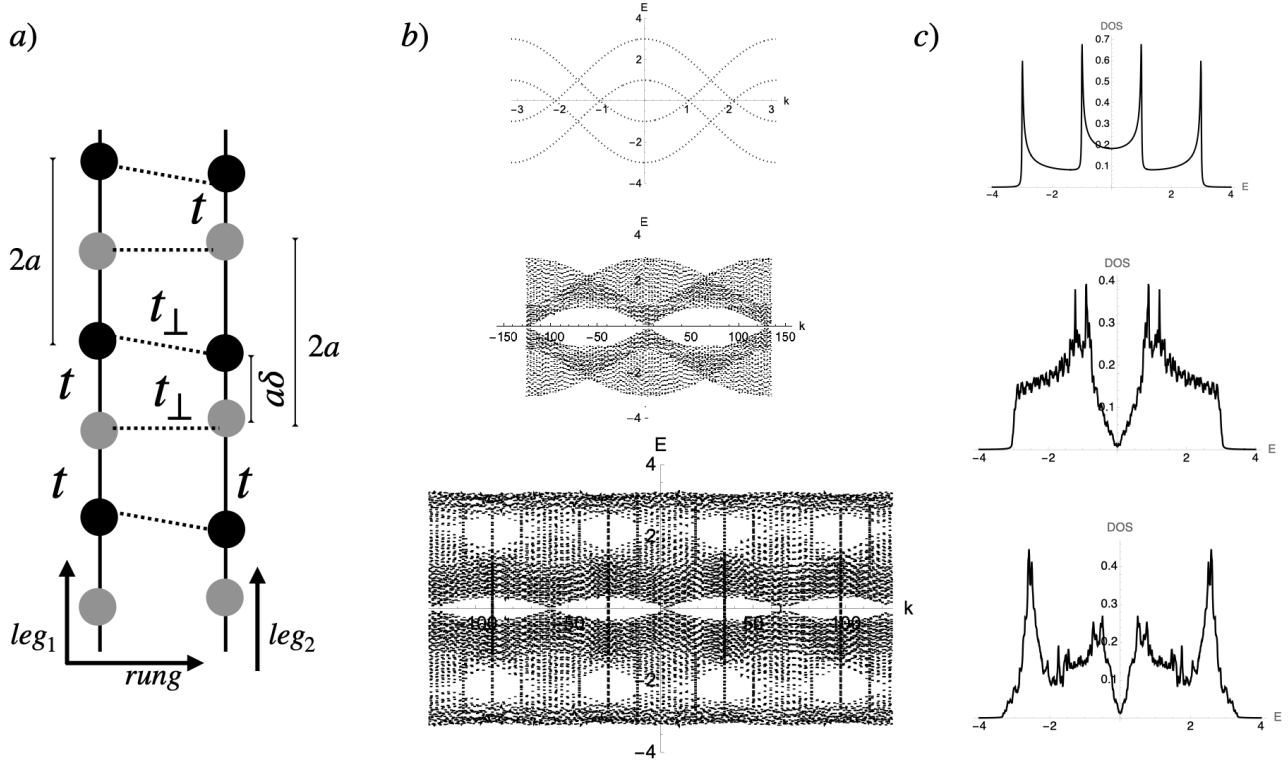


FIG. 1. (a) Illustration of the moiré ladder system. (b) Band spectra in the EBZ of $H(k)$, of a spinless system at $\delta = 1$ (upper panel), a spinless system at $\delta = \frac{19}{20}$ (middle panel) and of a spinful system with $\alpha = t$ at $\delta = \frac{19}{20}$ (lower panel). Without SOC, the spectrum consists of spin-degenerate moiré minibands with periodicity set by the superlattice reciprocal vector. With SOC ($\alpha = t$), spin degeneracy is lifted and multiple avoided crossings appear. The effective periodicity of the spectrum in the EBZ is reduced by a factor of two, reflecting the breaking of pure translational symmetry by momentum-odd Rashba SOC. (c) DOS at $T=0$ of a spinless system with $\delta = 1$ (upper panel), a spinless system with $\delta = \frac{19}{20}$ (middle panel) and a spinful system $\alpha = t$ at $\delta = \frac{19}{20}$ (lower panel).

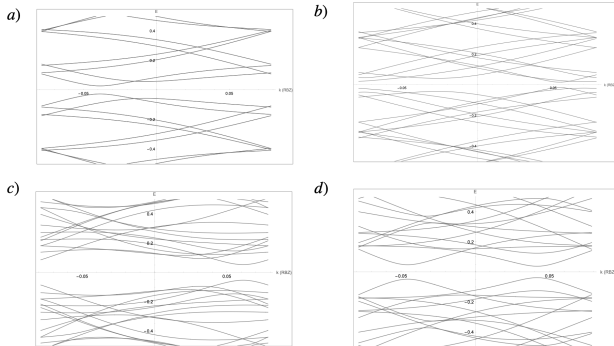


FIG. 2. Zoom out of the spectrum of the minibands in the RBZ (close to the fermi energy ($E=0$)). (a,b) spectrum of the system at $\delta = \frac{19}{20}$ and $\alpha = t$ without (a) and with (b) SOC. (c,d) spectrum of the system at $\delta = \frac{17}{20}$ and $\alpha = t$ without (c) and with (d) SOC.

II. MODEL

We model TI/Gr heterostructures as a ladder system, where the top and bottom legs represent the top and

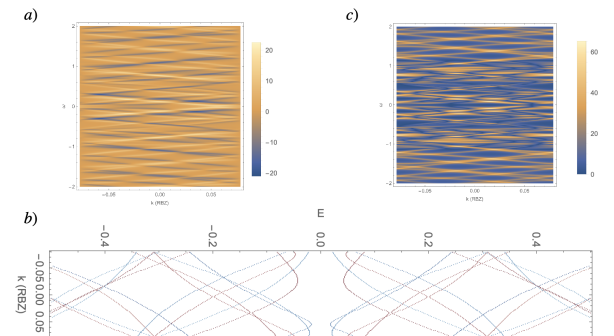


FIG. 3. (a) Helical spectral function of the system at $\delta = \frac{19}{20}$, $\alpha = t$ and $T = 0$. (b) zoom out of the minibands spectrum close to the fermi energy ($E=0$) at $\delta = \frac{19}{20}$, $\alpha = t$. The colors of the minibands reflect their helicity weight. (c) Helicity current spectral function at $\delta = \frac{19}{20}$, $\alpha = t$ and $T = 0$.

bottom surfaces of the heterostructure, as illustrated in Fig.1(a). Each ladder has two sites (A and B representing two different atoms) per unit cell, and the composite ladder unit cell contains a total of four sites $\{A_1, B_1, A_2, B_2\}$

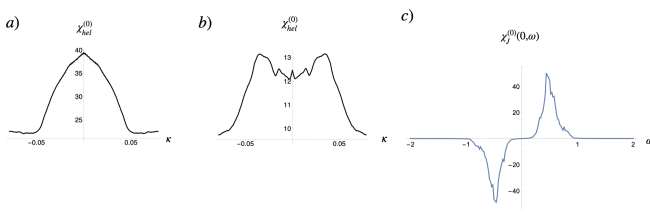


FIG. 4. (a-b) Lindhard susceptibility of the system with $\alpha = t$ and $T = 0$ at (a) $\delta = \frac{19}{20}$ and (b) $\delta = \frac{17}{20}$. (c) Dynamical susceptibility of the helicity current operator of the system with $\alpha = t$ and $T = 0.1$ at $\delta = \frac{17}{20}$.

(subscripts 1, 2 label legs). The composite cell has a length equal to $2a$, and the original reciprocal period is $G_0 = \pi/a$. Henceforth, we choose half of the legs lattice constant as the length unit.

The two-leg ladder is subject to moiré modulation due to the slight dimerization in leg-2 as shown in Fig.1(a). The microscopic tight-binding Hamiltonian for spinful fermions formulated in the extended Brillouin zone (EBZ), contains eight bands due to leg, orbital, and spin degrees of freedom. The fermionic operators are defined as $c_{j,\ell,\sigma}$, where $\ell = 1, 2$ labels the leg and $\sigma = \uparrow, \downarrow$ is the spin quantized along the z axis. The Hamiltonian is written as

$$H = H_K + H_{\text{SOC}}, \quad (1)$$

with $H_K = H_{\parallel} + H_{\perp}$ the contribution from the kinetic energy along the ladder. It comprises an intra-leg nearest neighbor hopping term, H_{\parallel} given by

$$H_{\parallel} = \sum_{j,\ell,\sigma} -t_{\parallel} \left(c_{j+1,\ell,\sigma}^{\dagger} c_{j,\ell,\sigma} + \text{h.c.} \right), \quad (2)$$

In Eq.2, the tunneling amplitude in leg-1 t_{\parallel} is a constant $t_{\parallel} = t$. However, in leg-2, the hopping amplitude depends on the dimerization parameter δ and acquires a phase $e^{-i\pi\delta}$ [20].

The inter-leg (rung) hopping term between nearest neighbor atoms in the same sublattice is

$$H_{\perp} = \sum_{j,\sigma} t_{\perp}(j) \left(c_{j,1,\sigma}^{\dagger} c_{j,2,\sigma} + \text{h.c.} \right), \quad (3)$$

The rung tunneling acquires a moiré periodicity inherited from the commensuration between the two legs, a product of the dimerization of leg-2.

The last term in Eq.1 consists of a SOC contribution in each leg that locks spin polarization along the y direction.

To ensure that the moiré modulation is commensurate, we set $\delta = p/q$ with coprime integers p and q , so that both the interleg modulation and the leg-2 dimerization become periodic over q unit cells (for example, for $\delta = \frac{19}{20}$, the corresponding supercell spans 20 unit cells). The relative mismatch between legs yields a moiré supercell of q

composite cells with $4q$ sites in total, a moiré reciprocal vector in the reduced Brillouin zone (RBZ) $b_s = \frac{G_0}{q} = \frac{\pi}{q}$, and a real-space supercell length $L_s = 2q$. The intra-leg nearest neighbor hopping, t , sets the bandwidth $W \sim 4t$. Rung tunneling has an average of t . Schrieffer-Wolff perturbation theory [23] gives rise to a first-harmonic rung tunneling of amplitude $t_1 = (1 - \delta)t$ modulated by the envelope $t_{\perp}(n) = t + t_1 \cos\left(\frac{2\pi n}{q}\right)$. Structure factors associated with hopping in leg-1 and leg-2 are respectively $co(k) = 2\cos k$, $co_{\delta}(k) = 2\cos(k - \pi\delta)$, and the Peierls phase from the dimerization of leg-2 is $\phi(k) = k(1 - \delta) + \pi\delta$. In Fourier space, the moiré rung modulation becomes $t_{\perp}(k) = 1 + (1 - \delta)\cos(qk)$. Throughout, we choose t as our energy scale.

In graphene-based heterostructures coupled either to a topological insulator or to a substrate that induces a perpendicular electric field, the dominant proximity-induced SOC is generally of Rashba character [24]. Microscopically, this Rashba SOC originates from virtual hopping processes, during which an electron experiences a momentum-dependent spin rotation as it moves in the gradient of the interfacial electric field normal to the heterostructure plane [25, 26]. In a quasi-one-dimensional lattice description, the Rashba SOC generated by a perpendicular electric field $\mathbf{E} = E_z \hat{z}$ takes the form

$$H_{\text{SOC}} = \alpha \sum_j \left(c_{j+1}^{\dagger} i\sigma_y c_j - c_j^{\dagger} i\sigma_y c_{j+1} \right), \quad (4)$$

where the fermion operators $c_j = (c_{j\uparrow}, c_{j\downarrow})^T$ and σ_y act on spin. This expression embodies how Rashba SOC ties the electron spin to its bonding direction via the interfacial electric field. Fourier transforming Eq. (4), one obtains

$$H_{\text{SOC}}^{(1)} = 2i\alpha \sum_k (\sin k) c_k^{\dagger} \sigma_y c_k. \quad (5)$$

In a uniform system such as leg-1, the SOC term in Eq.5 appears as a momentum-odd contribution proportional to $\sin k$, which vanishes at time-reversal invariant momenta and reflects the inversion-symmetry breaking at the interface.

In leg-2 where the parameter δ , effectively shifts the crystal momentum by a fraction of the reciprocal lattice vector, the hopping paths of electrons are modulated in real space. As a result, the SOC term on that leg acquires a phase,

$$H_{\text{SOC}}^{(2)} = \alpha \sum_j \left(e^{-i\pi\delta} c_{j+1,2}^{\dagger} i\sigma_y c_{j,2} - e^{+i\pi\delta} c_{j,2}^{\dagger} i\sigma_y c_{j+1,2} \right),$$

Fourier transforming the previous equation yields

$$H_{\text{SOC}}^{(2)} = 2i\alpha \sum_k e^{i\phi(k)} \sin(k - \pi\delta) c_{k,2}^{\dagger} \sigma_y c_{k,2}. \quad (6)$$

with α the SOC strength and $\sigma_y = \begin{pmatrix} 0 & -i \\ i & 0 \end{pmatrix}$. We define the spinor in the leg/site/spin basis

as the following eight-component object, $\Psi_k = (c_{1,A\uparrow}, c_{1,A\downarrow}, c_{1,B\uparrow}, c_{1,B\downarrow}, c_{2,A\uparrow}, c_{2,A\downarrow}, c_{2,B\uparrow}, c_{2,B\downarrow})$.

To model the two surfaces of the heterostructure, we assign opposite helicity to the two legs: leg 1 carries helicity $+\sigma_y$ (upper surface) and leg 2 carries helicity $-\sigma_y$

$$H(k) = \begin{pmatrix} 0 & 0 & co(k) & -is(k) & t_{\perp}(k) & 0 & 0 & 0 \\ 0 & 0 & is(k) & co(k) & 0 & t_{\perp}(k) & 0 & 0 \\ co(k) & -is(k) & 0 & 0 & 0 & 0 & t_{\perp}(k) & 0 \\ is(k) & co(k) & 0 & 0 & 0 & 0 & 0 & t_{\perp}(k) \\ t_{\perp}(k) & 0 & 0 & 0 & 0 & 0 & 0 & 0 \\ 0 & t_{\perp}(k) & 0 & 0 & 0 & 0 & -is_{\delta}(k) e^{-i\phi(k)} & co_{\delta}(k) e^{i\phi(k)} \\ 0 & 0 & t_{\perp}(k) & 0 & co_{\delta}(k) e^{-i\phi(k)} & is_{\delta}(k) e^{i\phi(k)} & 0 & 0 \\ 0 & 0 & 0 & t_{\perp}(k) & -is_{\delta}(k) e^{-i\phi(k)} & co_{\delta}(k) e^{-i\phi(k)} & 0 & 0 \end{pmatrix}, \quad (7)$$

where $s(k) = 2\alpha \sin k$ and $s_{\delta}(k) = 2\alpha \sin(k - \pi\delta)$. Eq.7 is given in the extended Brillouin zone (EBZ), $k \in (-qG_0, qG_0)$. For a given δ , the similarity transformation $\Delta = \pi q$ applied to $H(k)$ imposes constraints on p and q that determine the generic global period $2\pi q$ giving rise to EBZ [20]. On the other hand, the reduced first Brillouin zone of the moiré lattice (RBZ) spans the interval $(-b_s/2, b_s/2)$, and the reciprocal superlattice $G_s = \{m b_s \mid m \in \mathbb{Z}\}$ as we detail below.

III. ENERGY SPECTRUM AND DENSITY OF STATES

We have recently shown that the inclusion of moiré modulation in a moiré two leg ladder has a large effect on the bands and density of states (DOS) [22]. The spectrum (which is exactly solvable) of Eq.7, in the EBZ, is presented Figure 1. Fig.1b compares the energy spectrum in the extended Brillouin zone for a modulated system at $\delta = 0.95$, in the absence and presence of spin-orbit coupling. In the SOC-free case ($\alpha = 0$, middle panel), the spectrum consists of a dense set of folded minibands originating from the moiré modulation. The bands remain spin-degenerate throughout the EBZ, and a tiny gap visible around the Fermi energy, $E=0$, is a direct consequence of δ , which breaks the translational symmetry. Minigaps at folded-band crossings are apparent and scale linearly with t_1 at small modulation (large δ). Upon turning on SOC ($\alpha = t$), the overall band structure is preserved, indicating that SOC does not qualitatively alter the moiré folding. However, SOC lifts the spin degeneracy and gaps out a fraction of the band crossings, producing a fine pattern of avoided crossings across the EBZ (lower panel). Due to the moiré potential, the spin character is redistributed across the miniband manifold, even though no large global gap opens.

In the absence of SOC, the spectrum obeys $E(k) = E(k + G_m)$. Once Rashba SOC is introduced, the Hamil-

(lower surface). The upper two orbitals (leg 1) thus experience a potential $+2i\alpha \sin k \sigma_y$, while the lower two orbitals (leg 2) experience $-2i\alpha \sin(k - \pi\delta) \sigma_y$. The total Hamiltonian, including both the kinetic terms and the opposite-helicity spin-orbit coupling, yields

tonian acquires momentum-odd contributions $\propto \sin(k - \pi\delta) \sigma_y$, which reverse sign under $k \rightarrow k + G_m$. Consequently, translation by G_m alone ceases to be a symmetry. The Hamiltonian remains invariant only under the combined action of a moiré translation and a π spin rotation about the y axis. Because this composite symmetry squares to a translation by $2G_m$, the spectral periodicity in the extended Brillouin zone is effectively halved, accounting for the reduced EBZ period observed in the lower panel of Fig.1(b).

With a perfect match between the legs ($\delta = 1$), the DOS shown in the upper panel of Fig.1 depicts a pair of van Hove singularities (VHS) at the edges of the bands, a finite density of states at all energies, and another pair of VHS at $E = \pm t_1$, signaling the coupling between the two legs. Once $\delta \neq 1$, the moiré potential smears out the peaks at the edges of the spectra; the VHS at $E = \pm t$ splits into two peaks about $E \sim \pm t_1$ due to the breaking of inversion symmetry (middle panel); and the DOS $\sim \eta$ at the Fermi energy as the system becomes gapped [27]. Including SOC (lower panel) removes spin degeneracy, opening gaps at many band crossings, redistributing spectral weight, and producing a qualitatively altered DOS. Sharp peaks broaden or split, and new fine structures emerge due to SOC-driven avoided crossings.

To build the Hamiltonian of the system in the RBZ we keep the q replica momenta $\{\bar{k} + mG_s\}_{m=0}^{q-1}$ in the Hamiltonian matrix H_{RBZ} . Thus, the block-diagonal piece becomes $[H_{\text{RBZ}}^{(0)}(\bar{k})]_{mm'} = \delta_{mm'} H(\bar{k} + mG_s)$, $m, m' = 0, \dots, q-1$. Rung modulation $\cos(qk)$ connects nearest-neighbor replicas in the RBZ and gives rise to the off-diagonal part $[\delta H_{\text{RBZ}}(\bar{k})]_{m, m \pm 1} = \frac{t_1}{2} R$, $R = \sigma_1 \otimes \mathbb{I}_2$, where σ_j is the j -th Pauli matrix. The $4q \times 4q$ moiré Hamiltonian in the RBZ becomes [20] $H_{\text{RBZ}}(\bar{k}) = H_{\text{RBZ}}^{(0)}(\bar{k}) + \delta H_{\text{RBZ}}(\bar{k})$. If $t_1 = 0$ the $4q$ bands split into q independent copies of the four parent bands evaluated at $\bar{k} + mG_s$. The symmetry of H is preserved by H_{RBZ} [20].

Fig.2 shows a zoomed-out view of the energy spectra of

the minibands in the reduced Brillouin zone at $\delta = 0.95$ and $\delta = 0.85$ in the absence (a,c) and presence (b,d) of spin-orbit coupling. Without SOC, the RBZ spectrum consists of multiple folded minibands that intersect extensively, reflecting both the moiré backfolding and the underlying spin degeneracy. Figs.2(b,d) show that SOC qualitatively restructures the internal organization of the minibands: spin degeneracy is lifted, and a large fraction of the band crossings are replaced by avoided crossings. As a result, the RBZ spectrum becomes more densely interconnected, with miniband branches hybridizing over extended momentum ranges. This reconstruction reflects the entanglement of spin and moiré degrees of freedom induced by SOC and leads to a redistribution of spectral weight across the miniband manifold.

The Dirac-like crossings observed in Fig.2(d) indicate that the moiré modulated SOC not only lifts degeneracies, but also reorganizes the miniband structure into effective two-band sectors with linear dispersion. The case at $\delta = 0.85$ illustrates how moiré modulation and SOC jointly induce emergent relativistic behavior in otherwise heavily folded miniband spectra. A symmetry mechanism is expected to safeguard the Dirac-type band crossings in the RBZ spectrum when SOC is included. With SOC present, a pure moiré translation by a reciprocal lattice vector G_m ceases to be a symmetry since the Rashba-like SOC term is odd in momentum and reverses sign under $k \rightarrow k + G_m$. Nevertheless, the Hamiltonian is invariant under the composite operation $\tilde{T} = T_{G_m} \mathcal{R}_y(\pi)$, with $\mathcal{R}_y(\pi) = -i\sigma_y$ denoting a π spin rotation about the SOC-defined axis. This combined spin-translation symmetry yields $\tilde{T}^2 = T_{2G_m}$, thereby halving the fundamental periodicity of the EBZ. \tilde{T} acts as a quantum number that differentiates miniband eigenstates, such that bands with distinct \tilde{T} eigenvalues cannot hybridize at the same momentum. As a result, when moiré folding brings bands from different \tilde{T} sectors into contact, SOC imposes symmetry-protected linear crossings, yielding Dirac-like nodes in the miniband spectrum.

IV. HELICAL MODES

Helical states have been observed in moiré heterostructures featuring proximity induced SOC [28–32]. In spin-orbit coupled systems, helicity refers to the projection of the spin degree of freedom onto a momentum and symmetry defined internal axis. For continuum Rashba models, it is typically specified as the eigenvalue of $\hat{\sigma} \cdot (\hat{z} \times \hat{k})$ [1], which quantifies the locking between spin and momentum. In our moiré ladder framework, we define the helicity operator as the difference between the spin densities on the two legs [33],

$$\Gamma_{\text{hel}} = S_y^{(1)} - S_y^{(2)}, \quad (8)$$

where

$$S_y^{(\ell)} = \sum_k c_{k,\ell}^\dagger \sigma_y c_{k,\ell}, \quad (9)$$

with σ_y acting in spin space. With this definition, helicity quantifies how unevenly spin polarization along the SOC-determined axis is shared between the two legs. The corresponding operator is antisymmetric under leg exchange, invariant under time reversal, and zero when SOC is absent due to spin-rotation symmetry.

In order to find out whether Γ_{hel} appears in single-particle states, we compute the dynamical spectral function in the system using Lorentzian broadening: $A_\Gamma(k, \omega) = \sum_n |\langle n, k | \Gamma | n, k \rangle|^2 \frac{\eta}{(\omega - E_{n,k})^2 + \eta^2}$, where η is a small positive broadening. The helicity-resolved spectral function offers a direct probe of how proximity-induced spin-orbit coupling is redistributed throughout the moiré minibands. Without spin-orbit coupling, spin-rotation symmetry enforces the helicity-resolved spectral function to be zero. Upon introducing SOC, Fig.3a reveals a dense mesh of oblique streaks with alternating blue and white intensities spanning the reduced Brillouin zone. Each streak represents a miniband branch with nonzero helicity weight, where the color encodes both the sign and magnitude of the expectation value of the helicity operator Γ_{hel} . The tilted alignment of these features arises from the finite group velocity of the associated states, and the alternating sign directly evidences spin-momentum locking: minibands with opposite dispersion slopes possess opposite helicity, as enforced by time-reversal symmetry.

Unlike uniform Rashba systems, where helicity is restricted to a few well-defined branches, the moiré potential distributes helicity across numerous minibands. The color-coded miniband structure in the RBZ in Fig.3b shows that every miniband branch in the reduced Brillouin zone carries nonzero helicity weight. The simultaneous presence of positive and negative helicity on different branches reflects the odd-momentum character of the SOC and the maintenance of time-reversal symmetry.

Examining the helicity current is particularly relevant in systems with proximity-induced spin-orbit coupling, where spin-momentum locking enables these internal spin textures to influence quasiparticle dynamics even when there is no net charge or spin flow [34, 35]. The helicity current operator is defined as the symmetrized product of the velocity operator and the helicity density,

$$J_{\text{hel}}(k) = \frac{1}{2} \{v(k), \Gamma_{\text{hel}}\}, \quad (10)$$

where $v(k) = \partial H(k) / \partial k$ denotes the band velocity operator. Fig.3c shows a dense array of tilted streaks with alternating signs and magnitudes. Each streak represents a dispersive miniband that carries a finite helicity current, whose sign is fixed by the interplay between the group velocity and helicity polarization. Time-reversal symmetry requires the presence of counterpropagating channels with opposite helicity current, producing the characteristic interlaced pattern throughout the reduced Brillouin zone. Analogous to helicity density, moiré-driven miniband hybridization disperses the helicity current over the full spectrum instead of confining it to a few Rashba-like

branches.

Fig.3b shows that no minibands remain helicity-silent. Therefore, fluctuations in the helicity order parameter can be derived from an extensive set of particle-hole excitations involving all minibands, making the system intrinsically prone to helical collective behavior.

V. HELICAL FLUCTUATIONS

The tendency toward instability in the helicity channel is captured by the associated two-particle response function. To characterize how strongly the system favors forming a helicity modulation with wavevector κ , we apply an external (generalized) field $h(\kappa)$ that couples linearly to the helicity density operator $\Gamma_{\text{hel}}(\kappa)$ [36]. The resulting Hamiltonian takes the form

$$H_h = H - \sum_{\kappa} h(\kappa) \Gamma_{\text{hel}}(-\kappa), \quad (11)$$

where H denotes the unperturbed single-particle Hamiltonian, and $\Gamma_{\text{hel}}(\kappa)$ represents the Fourier component of

the helicity density. Within linear response theory, the induced expectation value is connected to the external field via

$$\delta \langle \Gamma_{\text{hel}}(\kappa) \rangle = \chi_{\text{hel}}(\kappa, \omega) h(\kappa, \omega), \quad (12)$$

with the susceptibility defined by the Kubo formula [37]

$$\chi_{\text{hel}}(\kappa, \omega) \equiv -i \int_0^{\infty} dt e^{i(\omega+i0^+)t} \langle [\Gamma_{\text{hel}}(\kappa, t), \Gamma_{\text{hel}}(-\kappa, 0)] \rangle. \quad (13)$$

Here $\Gamma_{\text{hel}}(\kappa, t) = e^{iH_0t} \Gamma_{\text{hel}}(\kappa) e^{-iH_0t}$ is the Heisenberg operator, and $\langle \dots \rangle$ denotes a ground-state expectation value. The static helicity susceptibility corresponds to the zero-frequency limit,

$$\chi_{\text{hel}}(\kappa) \equiv \chi_{\text{hel}}(\kappa, \omega=0) = \lim_{\omega \rightarrow 0} \chi_{\text{hel}}(\kappa, \omega). \quad (14)$$

With the sign convention used in this work (so that a positive χ corresponds to an enhancement of helicity fluctuations), we finally write [37]

$$\chi_{\text{hel}}^{(0)}(\kappa) = -\frac{1}{N_k} \sum_{k,n,m} \frac{f(E_n(k)) - f(E_m(k+\kappa))}{E_n(k) - E_m(k+\kappa)} |\langle n, k | \Gamma_{\text{hel}} | m, k+\kappa \rangle|^2, \quad (15)$$

where $E_n(k)$ are the miniband energies, and $f(E)$ is the Fermi-Dirac distribution at finite temperature T . A pronounced maximum in $\chi_{\text{hel}}^{(0)}(\kappa)$ indicates collective fluctuations in the helicity channel and reveals the characteristic momentum profile of the leading helical mode. This determines whether the noninteracting band structure shaped by moiré modulation and proximity-induced SOC is inherently inclined toward helical instabilities, thereby supplying the microscopic basis for helical phases to develop once additional symmetry-breaking fields or interactions are applied.

Fig.4(a,b) presents the helical susceptibility for $\delta = \frac{19}{20}$

and $\delta = \frac{17}{20}$ at $\alpha = t$. For $\delta = 0.95$, a pronounced maximum appears at $\kappa = 0$, indicating a propensity toward a uniform helical phase. Lowering the modulation to $\delta = 0.85$ substantially alters the profile of the static helicity susceptibility $\chi_{\text{hel}}(\kappa)$. For stronger modulation, the uniform mode at $\kappa = 0$ persists, but the susceptibility exhibits pronounced symmetric peaks at $\pm\kappa^*$, demonstrating that the leading helical fluctuations are shifted to a finite wave vector. This behavior marks a transition from an essentially uniform helicity response to an emerging helical density-wave state.

In order to probe frequency resolved fluctuations of helicity transport [34, 38], we consider the dynamical susceptibility associated with the helicity current operator.

$$\chi_J^{\text{hel}}(\kappa, \omega) = \sum_{k,n,m} \frac{f(E_n(k)) - f(E_m(k+\kappa))}{\omega + i\eta + E_{kn} - E_{k+\kappa,m}} |\Gamma_{J,nm}^{\text{hel}}(k, k+\kappa)|^2,$$

which is the retarded current-current correlator. The vertex $\Gamma_{J,nm}^{\text{hel}}(k, k+\kappa) = \langle n, k | \hat{J}_{\text{hel}}(k) | m, k+\kappa \rangle$ is the momentum dependent helicity current matrix element. The imaginary part of the susceptibility, $\Im \chi_J^{\text{hel}}(\kappa, \omega)$, represents the absorption spectrum of helicity current

fluctuations [36] and quantifies the phase space of particle-hole excitations [38], thereby capturing both the band-structure kinematics and the internal helicity texture of the minibands.

Figure 4(c) shows $\Im \chi_J^{\text{hel}}(q = 0, \omega)$ computed at $\delta =$

0.85 for $\alpha = t$, and $T = 0.1$. The mirror feature at negative frequencies follows from the antisymmetry of the imaginary part. The strong peaks at low positive frequencies arises from low-energy interband particle-hole excitations between moiré minibands, whose energies are brought close by the modulation and further reshaped by spin-orbit coupling. The helicity current vertex significantly amplifies these transitions, producing a pronounced finite frequency response even at zero momentum.

VI. CONCLUSIONS

To explore how proximity-induced spin-orbit coupling in TI/graphene interfaces relates to the moiré potentials arising at heterostructure interfaces, we have studied a toy model of a ladder system with moiré modulation, in which the spin-orbit interaction acquires the moiré modulation through a slight dimerization of one ladder leg.

Without SOC, the spectrum is formed by spin-degenerate moiré minibands whose periodicity is fixed by the superlattice folding. Incorporating SOC removes the spin degeneracy and reduces the effective spectral periodicity in the EBZ by a factor of two. This reduction arises from the momentum-odd Rashba SOC, which destroys the equivalence of states connected by the original moiré translation.

The moiré parameter δ compresses the electronic spectrum into narrow minibands and increases the density of states near the Fermi level. Moiré modulated SOC entangles spin, sublattice, and leg degrees of freedom, reshaping the miniband structure in momentum space instead of inducing a simple rigid spin splitting. As a

consequence it gives rise to emergent helicity spectral functions absent in uniform systems. We found that helicity weight spreads over a dense manifold of moiré minibands, forming an extended network of helicity-carrying states rather than being confined to a few Rashba-like branches. The concurrent halving of the effective EBZ periodicity and the emergence of numerous SOC-driven avoided crossings signals a profound reorganization of momentum-space symmetry. Because positive and negative helicity sectors coexist at the same energy, the total helicity current cancels in equilibrium, despite a large local helicity-resolved spectral weight. The helicity spectral function therefore captures internal spin-leg textures and fluctuations rather than transport.

The appearance of Dirac-like miniband crossings at finite SOC shows that moiré heterostructures can host relativistic quasiparticles via band reconstruction, even when the underlying bands are nonrelativistic. Consequently, helicity-resolved static susceptibilities exhibit sharp peaks, revealing strong collective helicity fluctuations already at the bare-response level.

Our findings show that moiré heterostructures constitute an advantageous setting where proximity-induced SOC is not simply transferred from the interface, but significantly enhanced and reshaped through miniband hybridization, thereby strongly favoring the emergence of helical states when additional symmetry-breaking fields or interactions are applied.

ACKNOWLEDGMENTS

The author acknowledges support from the Fondo Nacional de Desarrollo Científico y Tecnológico (Fondecyt) under Grant No. 1250122.

[1] A. Manchon, H. C. Koo, J. Nitta, S. M. Frolov, and R. A. Duine, New perspectives for rashba spin-orbit coupling, *Nature materials* **14**, 871 (2015).

[2] A. Avsar, H. Ochoa, F. Guinea, B. Özyilmaz, B. Van Wees, and I. J. Vera-Marun, Colloquium: Spintronics in graphene and other two-dimensional materials, *Reviews of Modern Physics* **92**, 021003 (2020).

[3] M. Z. Hasan and C. L. Kane, Colloquium: topological insulators, *Reviews of modern physics* **82**, 3045 (2010).

[4] Z. Wang, D.-K. Ki, H. Chen, H. Berger, A. H. MacDonald, and A. F. Morpurgo, Strong interface-induced spin-orbit interaction in graphene on ws₂, *Nature communications* **6**, 8339 (2015).

[5] G. Rakhmanova and I. V. Iorsh, Broadband enhancement of second-harmonic generation at the domain walls of magnetic topological insulators, *Nanophotonics* **9**, 4489 (2020).

[6] M. Gmitra, D. Kochan, P. Högl, and J. Fabian, Proximity spin-orbit coupling physics of graphene in transition-metal dichalcogenides, in *Spin Orbitronics and Topological Properties of Nanostructures: Lecture Notes of the 12th International School on Theoretical Physics* (World Scientific, 2018) pp. 18–39.

[7] Y. S. Gani, E. J. Walter, and E. Rossi, Proximity-induced spin-orbit splitting in graphene nanoribbons on transition-metal dichalcogenides, *Physical Review B* **101**, 195416 (2020).

[8] K. Zollner, M. Gmitra, T. Frank, and J. Fabian, Theory of proximity-induced exchange coupling in graphene on hbn/(co, ni), *Physical Review B (PRB)* **94**, 155441 (2016).

[9] Y. Li and M. Koshino, Twist-angle dependence of the proximity spin-orbit coupling in graphene on transition-metal dichalcogenides, *Physical Review B* **99**, 075438 (2019).

[10] K. Premasiri and X. P. Gao, Tuning spin-orbit coupling in 2d materials for spintronics: a topical review, *Journal of Physics: Condensed Matter* **31**, 193001 (2019).

[11] T. Wakamura, F. Reale, P. Palczynski, M. Zhao, A. Johnson, S. Guérón, C. Mattevi, A. Ouerghi, and H. Bouchiat, Spin-orbit interaction induced in graphene by transition metal dichalcogenides, *Physical Review B* **99**, 245402

(2019).

[12] M. Yankowitz, S. Chen, H. Polshyn, Y. Zhang, K. Watanabe, T. Taniguchi, D. Graf, A. F. Young, and C. R. Dean, Tuning superconductivity in twisted bilayer graphene, *Science* **363**, 1059 (2019).

[13] R. Bistritzer and A. H. MacDonald, Moiré bands in twisted double-layer graphene, *Proceedings of the National Academy of Sciences* **108**, 12233 (2011).

[14] Y. Cao, V. Fatemi, A. Demir, S. Fang, S. L. Tomarken, J. Y. Luo, J. D. Sanchez-Yamagishi, K. Watanabe, T. Taniguchi, E. Kaxiras, *et al.*, Correlated insulator behaviour at half-filling in magic-angle graphene superlattices, *Nature* **556**, 80 (2018).

[15] E. Y. Andrei, D. K. Efetov, P. Jarillo-Herrero, A. H. MacDonald, K. F. Mak, T. Senthil, E. Tutuc, A. Yazdani, and A. F. Young, The marvels of moiré materials, *Nature Reviews Materials* **6**, 201 (2021).

[16] Y. Xiao, J. Liu, and L. Fu, Moiré is more: access to new properties of two-dimensional layered materials, *Matter* **3**, 1142 (2020).

[17] J. Zhang, C. Triola, and E. Rossi, Proximity effect in graphene-topological-insulator heterostructures, *Physical review letters* **112**, 096802 (2014).

[18] C.-C. Tseng, X. Ma, Z. Liu, K. Watanabe, T. Taniguchi, J.-H. Chu, and M. Yankowitz, Anomalous hall effect at half filling in twisted bilayer graphene, *Nature Physics* **18**, 1038 (2022).

[19] K. Zollner and J. Fabian, Bilayer graphene encapsulated within monolayers of ws 2 or cr 2 ge 2 te 6: Tunable proximity spin-orbit or exchange coupling, *Physical Review B* **104**, 075126 (2021).

[20] P. Mellado, F. Muñoz, and J. Cabezas-Escáres, Sliding phasons in moiré ladders, *arXiv preprint arXiv:2512.05735* (2025).

[21] Q. Gao and E. Khalaf, Symmetry origin of lattice vibration modes in twisted multilayer graphene: Phasons versus moiré phonons, *Physical Review B* **106**, 075420 (2022).

[22] P. Mellado, F. Muñoz, and J. Cabezas-Escáres, Excitonic charge density waves in moiré ladders, *arXiv preprint arXiv:2512.05696* (2025).

[23] S. Bravyi, D. P. DiVincenzo, and D. Loss, Schrieffer-wolff transformation for quantum many-body systems, *Annals of physics* **326**, 2793 (2011).

[24] G. Bihlmayer, P. Noël, D. V. Vyalikh, E. V. Chulkov, and A. Manchon, Rashba-like physics in condensed matter, *Nature Reviews Physics* **4**, 642 (2022).

[25] I. Ado, O. A. Tretiakov, and M. Titov, Microscopic theory of spin-orbit torques in two dimensions, *Physical Review B* **95**, 094401 (2017).

[26] L. Chen, M. Gmitra, M. Vogel, R. Islinger, M. Kronseder, D. Schuh, D. Bougeard, J. Fabian, D. Weiss, and C. Back, Electric-field control of interfacial spin-orbit fields, *Nature Electronics* **1**, 350 (2018).

[27] H. Ribeiro, K. Sato, G. Eliel, E. De Souza, C.-C. Lu, P.-W. Chiu, R. Saito, and M. Pimenta, Origin of van hove singularities in twisted bilayer graphene, *Carbon* **90**, 138 (2015).

[28] D. Khokriakov, A. M. Hoque, B. Karpak, and S. P. Dash, Gate-tunable spin-galvanic effect in graphene-topological insulator van der waals heterostructures at room temperature, *Nature communications* **11**, 3657 (2020).

[29] J. Kiemle, L. Powalla, K. Polyudov, L. Gulati, M. Singh, A. W. Holleitner, M. Burghard, and C. Kastl, Gate-tunable helical currents in commensurate topological insulator/graphene heterostructures, *ACS nano* **16**, 12338 (2022).

[30] K. Song, D. Soriano, A. W. Cummings, R. Robles, P. Ordejón, and S. Roche, Spin proximity effects in graphene/topological insulator heterostructures, *Nano letters* **18**, 2033 (2018).

[31] H. Li, H. Zhang, J. Shao, Y. Zhang, D. Yao, and G. Yang, Topological insulator-graphene junction for spin transport, *Applied Physics Letters* **101** (2012).

[32] M. A. Hoque, L. Sjöström, D. Khokriakov, B. Zhao, and S. P. Dash, Room temperature nonlocal detection of charge-spin interconversion in a topological insulator, *npj 2D Materials and Applications* **8**, 10 (2024).

[33] Y. A. Bychkov and E. I. Rashba, Oscillatory effects and the magnetic susceptibility of carriers in inversion layers, *Journal of physics C: Solid state physics* **17**, 6039 (1984).

[34] J. Sinova, D. Culcer, Q. Niu, N. Sinitsyn, T. Jungwirth, and A. H. MacDonald, Universal intrinsic spin hall effect, *Physical review letters* **92**, 126603 (2004).

[35] E. I. Rashba, Spin currents in thermodynamic equilibrium: The challenge of discerning transport currents, *Physical Review B* **68**, 241315 (2003).

[36] A. L. Fetter and J. D. Walecka, *Quantum theory of many-particle systems* (Courier Corporation, 2012).

[37] G. D. Mahan, Strong correlations, in *Many-Particle Physics* (Springer, 2000) pp. 375–432.

[38] A. Burkov and D. Hawthorn, Spin and charge transport on the surface of a topological insulator, *Physical review letters* **105**, 066802 (2010).